Planetary and Space Science 96 (2014) 71–80

Contents lists available at ScienceDirect

Planetary and Space Science

journal homepage: www.elsevier.com/locate/pss

Impact cratering experiments in brittle targets with variable thickness: Implications for deep pit craters on Mars

T. Michikami [a,*], A. Hagermann [b], H. Miyamoto [c], S. Miura [d], J. Haruyama [e], P.S. Lykawka [f]

[a] Faculty of Engineering, Kinki University, Hiroshima Campus, 1 Takaya Umenobe, Higashi-Hiroshima, Hiroshima 739-2116, Japan
[b] Department of Physical Sciences, The Open University, Walton Hall, Milton Keynes MK7 6AA, United Kingdom
[c] The University Museum, University of Tokyo, Hongo 7-3-1, Bunkyoku, Tokyo 113-0033, Japan
[d] Tokuyama College of Technology, Shunan, Yamaguchi 745-8585, Japan
[e] Institute of Space and Astronautical Science, Japan Aerospace Exploration Agency, Sagamihara, Kanagawa 252-8510, Japan
[f] Astronomy Group, Faculty of Social and Natural Sciences, Kinki University, Higashi-osaka, Osaka 577-0813, Japan

ARTICLE INFO

Article history:
Received 7 August 2013
Received in revised form
20 February 2014
Accepted 12 March 2014
Available online 25 March 2014

Keywords:
Impact cratering process
Pit crater
Penetration regime
Subsurface cavity
Laboratory experiments

ABSTRACT

High-resolution images reveal that numerous pit craters exist on the surface of Mars. For some pit craters, the depth-to-diameter ratios are much greater than for ordinary craters. Such deep pit craters are generally considered to be the results of material drainage into a subsurface void space, which might be formed by a lava tube, dike injection, extensional fracturing, and dilational normal faulting. Morphological studies indicate that the formation of a pit crater might be triggered by the impact event, and followed by collapse of the ceiling. To test this hypothesis, we carried out laboratory experiments of impact cratering into brittle targets with variable roof thickness. In particular, the effect of the target thickness on the crater formation is studied to understand the penetration process by an impact. For this purpose, we produced mortar targets with roof thickness of 1–6 cm, and a bulk density of 1550 kg/m^3 by using a mixture of cement, water and sand (0.2 mm) in the ratio of 1:1:10, by weight. The compressive strength of the resulting targets is 3.2 ± 0.9 MPa. A spherical nylon projectile (diameter 7 mm) is shot perpendicularly into the target surface at the nominal velocity of 1.2 km/s, using a two-stage light-gas gun. Craters are formed on the opposite side of the impact even when no target penetration occurs. Penetration of the target is achieved when craters on the opposite sides of the target connect with each other. In this case, the cross section of crater somehow attains a flat hourglass-like shape. We also find that the crater diameter on the opposite side is larger than that on the impact side, and more fragments are ejected from the crater on the opposite side than from the crater on the impact side. This result gives a qualitative explanation for the observation that the Martian deep pit craters lack a raised rim and have the ejecta deposit on their floor instead.

1. Introduction

Pit craters, pit chains, and trough-like depressions are commonly found on many solar-system bodies such as Mars (e.g., Banerdt et al., 1992; Wyrick et al., 2004; Cushing et al., 2007), the Moon (e.g., Head and Wilson, 1993; Haruyama et al., 2009, 2012; Robinson et al., 2012), the Earth (e.g., Okubo and Martel, 1998), Venus (e.g., Bleamaster and Hansen, 2004), Phobos (e.g., Thomas, 1979; Horstmann and Melosh, 1989), and asteroids (e.g., Prockter et al., 2002). Such pit-like depressions show appearances somehow similar to an impact crater, though they are typically steep-walled or composed of circular to elliptical depressions found in alignments or sometimes coalescing into linear troughs (Fig. 1). Deep pit craters frequently seen on Mars, are generally considered to be the results of roof collapses into subsurface cavities, which may be formed by lava tubes (Cushing et al., 2007), dike injection (Wilson and Head, 2002), extensional fracturing (Horstmann and Melosh, 1989), and dilational normal faulting (Ferrill et al., 2004).

Haruyama et al. (2009, 2012) and Martellato et al. (2013) indicated that the most plausible formation mechanism for Lunar deep pit craters is the formation of a skylight by collapse of the tube roof (We will call these 'Lunar deep pit craters' here, although they are often called 'Lunar deep pits' or 'Lunar holes'). One possibility suggested for their formation was the collapse of the tube roof brought about by a random meteoroid impact. Some pit craters (called Atypical Pit Craters by Cushing, 2012) on Mars are not associated with surface grooves and are nearly always circular with diameters of 80–300 m. Some of them (e.g., Fig. 1D and D′) are deep, sheer-walled cylindrical structures with no apparent subsurface extent. The shape of these pit craters is similar to that

* Corresponding author. Tel.: +81 824347000.
E-mail address: michikami@hiro.kindai.ac.jp (T. Michikami).

http://dx.doi.org/10.1016/j.pss.2014.03.010
0032-0633/

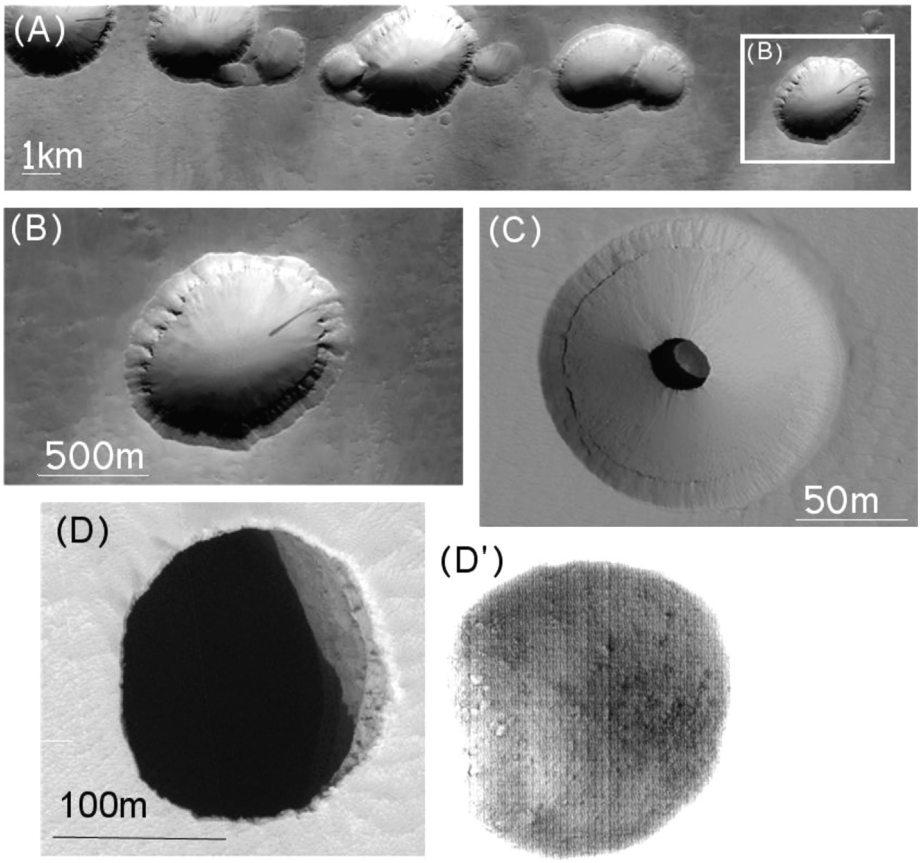

Fig. 1. Pit craters on Mars. (A) Pit crater chain in the south of Alba Patera, E0300254 (30.7°N, 246.3°E); (B) Close up of the marked pit crater in (A); (C) pit crater near the Pavonis Mons on Mars, possibly showing the formation stage of on-going ceiling collapse outward, ESP_023531_1840 (3.7°N, 248.5°E); (D) Pit crater 'Jeanne' near Arsia Mons, PSP_004847_1745 (5.5°S, 241.4°E); (D′) Another image of (D) that shows floor features in the shadow. Some boulders are seen on the floor.

of Lunar deep pit craters. Therefore, as one possibility, Martian deep pit craters might be produced by a random impact. Besides, Cushing (2012) reported about a pit crater at 3.7N, 248.5E on Mars (Fig. 1C), which appears to be a normal pit crater except that it has a central skylight entrance into a subsurface cavity. He also pointed out that it could represent an ongoing formation stage of ceiling collapse outward. The main crater has a raised rim which would be related to an impact origin. In this case, formational processes of pit craters and pit chains, or even some of trough-like depressions may be initiated by impact events.

In order to explore the possibility that formational processes of deep pit craters involve an impact event as an initiator of its formation, it is necessary to simulate an impact event onto the roof of a subsurface cavity. Laboratory experiment and computer simulation are the tools used to study impact crater formation; both have advantages and shortcomings. Laboratory experiments are limited to small scales, and extrapolation to planetary scales involves moving from a strength-dominated to a gravity-dominated regime. As an advantage of laboratory experiments, the impact conditions are controllable and results are reproducible (e.g., Housen and Holsapple, 1999). On the other hand, computer simulations offer great flexibility (e.g., Martellato et al., 2013), but it is difficult to verify a planetary scale impact, as no large-scale impact crater forming event has ever been observed on a solid target planetary body. However, it allows study of the dependence of cratering on various parameters, calculation of volume of impact melt, calculation of peak shock pressures, etc. Thus, both approaches offer insights into cratering which help clarify discussions of impact events (Burchell and Whitehorn, 2003).

Recently Martellato et al. (2013) carried out computer simulations to investigate the reliability of random meteoroid impacts as formation mechanism of Lunar skylights associated with the collapse of lava tube roofs. Their numerical simulations were performed considering basalts for both the projectile and the target material. The strengths (50 MPa) of their adopted basalt targets would be larger than that of the planetary surface, which is admittedly not very well characterized, but is thought to be on the order of 1 MPa (Melosh, 1989). The penetration process in basalt targets is considered to be different from that in brittle targets. Thus, we carry out laboratory impact experiments on brittle targets having variable roof thickness and strength of 1 MPa order.

What is of particular interest to us is the effect of brittle target thickness on crater formation so that we understand the condition for the transition from target cratering to target penetration. Most studies on laboratory impact experiments have focused on either cratering or catastrophic disruption. The intermediate regime between these two extremes (cratering and catastrophic disruption) has not been investigated to date; for brittle targets there is no experimental study regarding the effect of the target thickness on crater formation. Disruption of the target occurs when the shock waves from the impact travel and decay through the target body; the high pressure in a shock wave is relieved by the propagation of rarefaction. For impact cratering, the strength of the shock wave is generally attenuated until it subsides below the material strength of the target, and only the surface of the target is broken. Catastrophic disruption occurs when the strength of the shock wave at the opposite side of the impact (the back side of the target) is still larger than the material strength of the target. The ensuing rarefaction, which is the reflection of the shock wave, consequently disrupts the target. Thus, it is important to research the transition from target cratering to target penetration in terms of the propagation of rarefaction waves.

In this paper, as mentioned above, we explore the possibility that formational processes of deep pit craters involve an impact event. We therefore investigate the effect of the target roof thickness on crater shape by impact cratering experiments. Here, we assume two scenarios for the formation processes of deep pit craters related to an impact event. In *Scenario A*, the formation of a deep pit crater was triggered by an impact event, and followed by collapse of the ceiling. In this case, the crater rim might disappear due to this collapse. In *Scenario B*, a deep pit crater was produced by only one impact event, and there is no ensuing collapse of the ceiling. In Section 2, we describe the experimental method and target production. In Section 3, we present results in terms of shapes of the craters, the behavior of the excavation flow (ejection angle), and the antipodal velocity in the target. In Section 4, we compare the results of our experiments with those of experiments in other materials, and attempt to apply them to the deep pit craters observed on Mars. We discuss the two scenarios above and our experimental results. Finally, we present our conclusions in Section 5.

2. Experimental method

2.1. Target production

In order to simulate the formation of impact craters in cohesive and brittle material on Mars, the adopted targets were fabricated using a mixture of cement, water and 'Toyoura' sand (engineering standard-sand in Japan) in the ratio of 1:1:10, by weight. As the particle size is 0.2 mm, particle-scale inhomogeneities in the target were much smaller than the projectile size of 7 mm (the particle-to-projectile size ratio is about 0.029). The mixture was then put in a cylindrical mold 15 cm in diameter and was compacted. After a few days, the mold was taken off and the targets were left to air-dry for about one week. In the end, we produced cylindrical target blocks 15 cm in diameter and 6 cm high, with a bulk density of 1550 kg/m^3, and a porosity of 40%. The target surface is planar at the impact point. In order to investigate the influence of the target thickness on crater shape, a rectangular cavity was carved into the target underground to yield a cuboid as shown in Fig. 2. We produced targets with variable roof thickness (T_R=1, 2, 2.5, 3, 4 and 6 cm) and cavity widths (T_C=4 and 8 cm) (Table 1). This manufacturing process was chosen in order to prevent catastrophic failure of the targets from the vibration of the impact; experimental results using thin plate targets are not reported in this study because cracks radiate from the impact point in every direction and those targets are disrupted.

2.2. Strength testing

Several target samples were reserved for unconfined compressive strength testing. Cylindrical cores with a nominal size of 3.0 cm in length and 1.5 cm in diameter were drilled out from the targets, with their axes parallel to that of the cylindrical target. For strength testing, it is necessary to keep the contact surfaces at both ends of the sample core parallel to each other because a small difference in length of the cylindrical core brings about a large difference in compressive strength. Thus, we produced cylindrical cores of the same length within a precision of 0.10 mm.

The cores were placed in a load frame, which provided records of the force applied and the displacement of the moving crosshead. The unconfined compressive strength values were obtained using an *Autograph-5000A* [Shimazu Co, Ltd.]. The stress on the sample core was measured automatically at a constant displacement rate (1 mm/min). We measured compressive strength values ranging from 1.9 MPa to 4.5 MPa. The average value of measurements is 3.2 MPa and the standard deviation is 0.9 MPa. We also

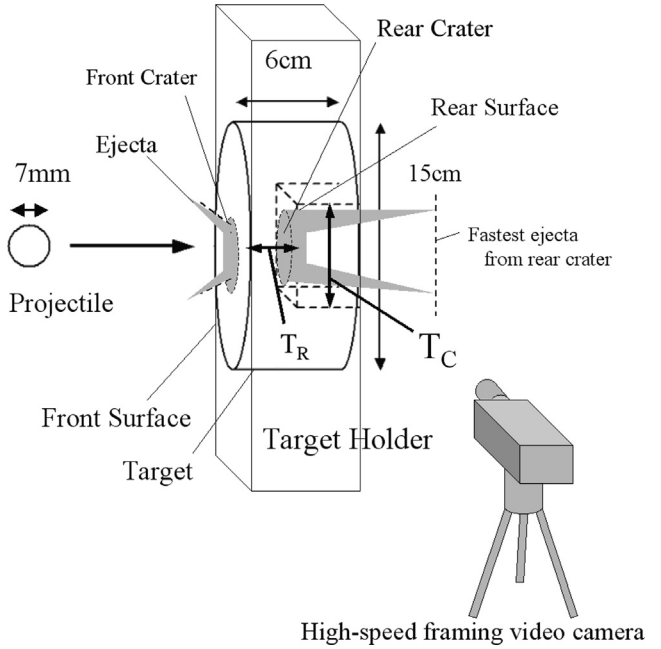

Fig. 2. Configuration of experimental setup. The targets were enclosed in a target holder with the front surface fully exposed to the impact and the rear surface partially exposed. The projectile approaches horizontally from the left and hits the flat surface of the cylindrical target at nominal velocity 1.2 km/s. T_R and T_C are defined as the target roof thickness and the width of cavity, respectively. Antipodal velocity is determined by measuring the velocity of the fastest ejecta from the rear crater using a high-speed framing video camera.

obtained stress–strain curves during the measurements. Several samples showed well-determined breaking points, sometimes along a diagonal plane from the edge on the top base to the opposite edge on the bottom base. Several other samples showed lower peak stress and small shape irregularities that caused the outer layers of the cylinder to spall off completely, leaving thin cores. This implies that, the compressive strength derived from strength tests contains an uncertainty caused by small shape irregularities of the sample core. Nevertheless, we believe the relevance of this uncertainty to be limited to the measuring stage. It certainly does not influence the outcome of the cratering experiments significantly, because we demonstrated the reproducibility of crater shapes in targets with identical shape to be good.

We also measured the tensile strength of a cylinder target with 10 cm in diameter and 8.7 cm in height using a cylinder splitting test, which is a tensile strength test widely used. The target tensile strength was 0.83 MPa, which is considered to be similar to the lithostatic stress pertinent to crater depths for 100 m-order sized craters on Mars (Ferrill et al., 2004).

Our strength tests essentially measured static strength. In impact experiments, however, it is the dynamic strength that matters (extremely high strain rate). The target strength in the dynamic regime is generally larger than that in the static regime (e.g., Housen and Holsapple, 1999). However, dynamic strength tests at high strain rate are very difficult to conduct for rocks and brittle targets. This is because, in most cases, existing experimental techniques will not allow maximum strain rates of 10^2 s^{-1} (e.g., Wang et al., 2006) to be reached, which is significantly lower than the strain rate on impact phenomena of planetary surface. To date, static strength tests are the standard method to measure material strength.

2.3. Impact experiments

A total of 20 impact experiments were carried out using a two-stage light-gas gun at the Institute of Space and Astronautical

Table 1
Target properties and experimental results, with values for T_R and T_C given in the first column. T_R=6 cm refers to targets without cavities (s63, s66, s72 and s76).

Shot number (T_R–T_C)	Hole Dia [mm]	Front Dia [mm]	Rear Dia [mm]	Front crater Depth [mm]	rear crater Depth [mm]	Impact Velocity [km/s]
s67(1–4)	20.5 ± 1.5	32.5 ± 1.5	42.0(max)	Hole	Hole	1.23
s69(1–4)	21.5 ± 1.5	36.0 ± 1.5	42.0(max)	Hole	Hole	1.21
s73(1–4)	23.5 ± 1.0	33.0 ± 2.0	51.0(max)	Hole	Hole	1.23
s82(1–4)*	21.0 ± 1.0	33.5 ± 2.0	49.0(max)	Hole	Hole	1.34
s71(1–8)	25.5 ± 2.0	42.0 ± 4.0	43.5 ± 1.5	Hole	Hole	1.25
s64(2–4)		34.0 ± 2.0	50.0(max)	7.5	11.0	1.20
s65(2–4)		30.5 ± 2.0	41.5(max)	5.5	7.5	0.96
s80(2–4)	10.5 ± 1.0	33.5 ± 4.5	53.0(max)	Hole	Hole	1.34
s68(2–8)	17.0 ± 1.0	34.5 ± 1.0	54.0 ± 3.0	Hole	Hole	1.30
s75(2–8)		33.5 ± 1.5	66.5 ± 3.5	8.0	11.0	1.20
s78(2–8)	10.5 ± 2.0	32.5 ± 2.0	54.0 ± 2.5	Hole	Hole	1.27
s81(2.5–8)		32.0 ± 2.0	63.0(max)	7.0	10.0	1.20
s77(3–4)		42.0 ± 4.0	60.0(max)	9.0	10.0	1.42
s79(3–8)		37.0 ± 3.0	72.5 ± 3.0	8.0	9.0	1.14
s70(4–4)		33.0 ± 2.5		6.0		1.15
s74(4–8)		37.0 ± 4.0		9.0		1.28
s63(6–0)		37.0 ± 1.0		7.5		1.41
s66(6–0)		37.5 ± 3.5		7.5		1.53
s72(6–0)		36.0 ± 2.5		7.0		1.22
s76(6–0)**		59.0 ± 2.0		13.0		2.70

* Only the experiment s82 was carried out with an impact angle of 45° relative to the target surface.
** Only the experiment s76 was carried out with the impact velocity of 2.70 km/s.

Science, Japan Aerospace Exploration Agency (ISAS, JAXA). Spherical nylon projectiles 7 mm in diameter (mass 0.213 g and density 1190 kg/m^3) were shot perpendicularly into the target surface at a nominal impact velocity of 1.2 km/s (Fig. 2 and Table 1). As an exception, only the experiment s76 was carried out with an impact velocity of 2.70 km/s.

Impact velocities were obtained from the passage time of the projectile between two laser beams. The targets were enclosed in a target holder with the front surface fully exposed on the impact side and the rear surface partially exposed on the opposite side. A high-speed framing video camera was used to record the motion of the fragments ejected from the target through the side windows of the chamber. The framing rate was 2000 frames per second and the field of view of the camera covered the entire inside chamber. Thus, we observed the motion of the fragments ejected from the front and the opposite sides. The whole system was mounted in a vacuum impact chamber with acrylic resin windows. The ambient pressure in the chamber was less than 200 Pa. For the targets with a roof thickness of 1 cm, 2 cm and 6 cm (i.e. without cavities), the experiments were carried out at least three times in order to confirm reproducibility. The reproducibility of our experiments was good (e.g., s67, s69 and s73), as differences in the impact outcomes were negligible.

3. Results

3.1. Crater

We observed a large span of crater shapes when using different roof thickness in targets. Fig. 3 shows examples of photographs and the related sketches of the craters obtained in our experiments (T_C=8 cm), and how crater shapes vary with the roof thickness T_R of the target (T_R=1–4 cm). The crater shapes obtained are similar in targets of identical shape. In Fig. 3, the crater shape for T_R=6 cm is not illustrated; it is, however, very similar to that for T_R=4 cm. In our experiments, we observed that a crater was produced on the opposite side of the target with respect to the impact for $T_R \leq 3$ cm. In the following, we refer to the crater formed on the impact surface as 'front crater' and to the crater formed on the opposite surface as 'rear crater'. Penetration of the target was achieved in thin targets (T_R=1 and 2 cm), when both of these craters were connected to form a continuous hole. Note that, for T_R=2 cm, we found targets with and without holes, indicating the transition from target cratering to target penetration.

The outlines of the front crater are seen in Fig. 3b. In general, the outline of the crater is formed by spallation (i.e. separation of relatively large fragments from a free surface as a result of dynamic tensile failure; e.g., Melosh, 1989). Therefore, the outline of the crater tends to be irregular due to the existence of incomplete spalls. Structurally strong targets such as basalt often show spallation. However, in our experiments, most of the outlines of the front crater are similar and irregular outlines occur only occasionally (the experiments s77 and s80). The reason for the lack of spallation in our experiments is probably due to the structural weakness of the targets.

In order to understand these craters shapes quantitatively, the diameters of the front crater, the rear crater and the hole are shown in Fig. 4. The diameter of front craters remains almost constant, regardless of target roof thickness and cavity width (Table 1). This implies that the cavity shape of the target does not affect the shape of the front crater, at least for 4 cm $\leq T_C \leq$ 8 cm. On the other hand, the rear crater diameters increase with target roof thickness, and are considerably larger than the diameters of the front craters in the targets with 1 cm $\leq T_R \leq$ 3 cm. In the case of targets with T_C=4 cm, a rear crater diameter has to be defined as the maximum size of the crater because the shape of the rear crater is occasionally an ellipsoidal (i.e. the rear crater is 'butterfly shaped' rather than circular), as a result of the restriction of the narrow cavity when T_C is 4 cm. The formation of the rear crater depends on the propagation and the strength of the rarefaction wave in the target, and will be described later in more detail.

As mentioned above, thin targets were penetrated when the front and rear craters were connected. To quantitatively confirm this result, we investigated the relationship between penetration hole and target thickness. For targets without a hole, the depth of the front (rear) crater is defined as the distance between the

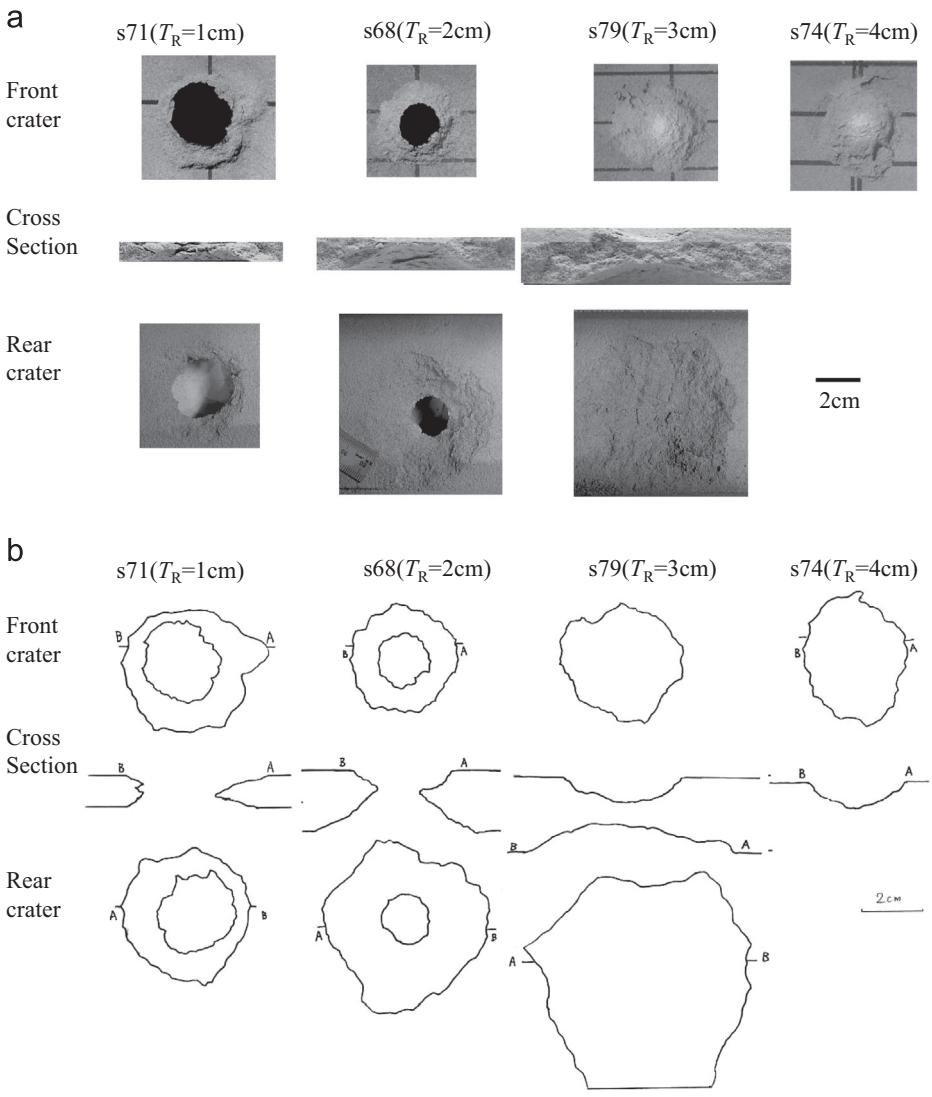

Fig. 3. (a)Examples of photographs of crater shapes (T_C=8 cm). Crater shapes are similar in targets of identical shape. Front crater, cross section and rear crater are shown in the photographs. The target roof thickness (T_R) is given in parentheses. (b) Examples of sketches of crater shapes (T_C=8 cm). The crater shape for T_R=6 cm, which is very similar to T_R=4 cm, is not illustrated.

pre-impact (the opposite pre-impact) surface and the crater floor. On the other hand, for targets with a hole, the depth of the front (rear) crater cannot be strictly defined because the crater floor is disrupted completely. We tried to estimate the depth of the front (rear) crater in targets with a hole, inferring the shape of the floor from the cross section of the crater. However, it is difficult to estimate the depth because the cross sections of the holes are complex. Therefore, we extrapolate the depths of the front and rear craters of the targets with a hole from those of the targets without a hole.

For front craters without a hole, the mean depth/diameter ratio is 0.21 $\pm$ 0.02, and is independent of T_R and T_C. The depth/diameter ratios for rear craters without a hole are slightly smaller, but also close to 0.2. As examples, in the case of targets close to the penetration transition and without a hole, the mean depth/diameter ratio for rear craters formed in targets with T_R=2 cm (s64, s65 and s75) is 0.19 $\pm$ 0.03, while the ratio for the rear crater with T_R=2.5 cm (s81) is 0.16. On the surfaces of the Moon and Mars, simple craters generally have the same depth/diameter ratio of 0.2 (e.g., Pike, 1977, 1988), although most of them are controlled by gravity. For the sake of simplicity, we use this ratio and define the quantity Q as the sum of the front crater and rear crater diameters multiplied by 0.2 (triangles in Fig. 5). Target thickness with and without holes is also illustrated in the same figure (filled and open circles). We can now quantify the necessary condition for target penetration as $Q > T_R$ i.e., targets are penetrated when front and rear craters are connected.

The transition from target cratering to target penetration at T_R=2 cm outlined above suggests that crater depth (of both front and rear crater) is sensitive to impact velocity. Table 1 shows that, for T_R=2 cm, targets are penetrated when the impact velocities are greater than 1.27 km/s. To confirm the dependence of impact velocity on crater depth, the experiments were carried out with impact velocities at 1.22, 1.41, 1.53 and 2.70 km/s for targets without cavities (T_R=6 cm; s72, s63, s66 and s76, respectively). The experimental results show that the depths of the front craters increase with increasing impact velocity. This reflects the fact that crater volumes are proportional to the impact energy, thus helping to penetrate the target. When no hole was obtained, only a very thin layer of target material remained between the front and the rear craters in targets with T_R=2 cm.

3.2. Ejecta mass and ejection flow

In order to investigate the amount of the fragments ejected from the front and the rear crater, the amount of ejecta in the chamber was measured. In our experiments, the ejecta collected

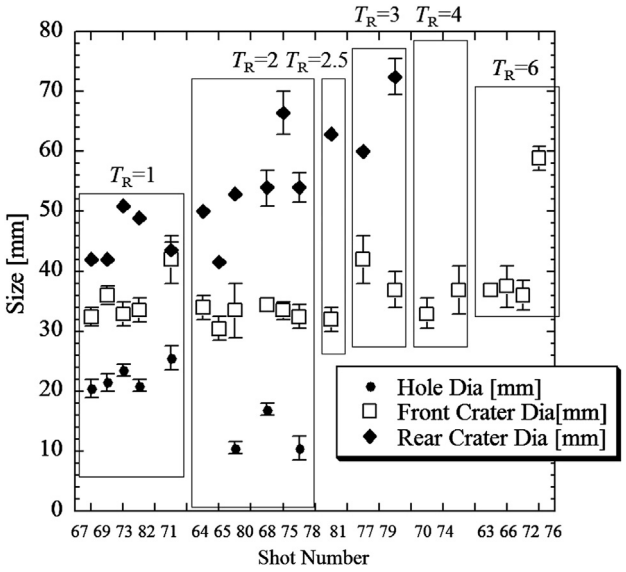

Fig. 4. Diameter of front crater (squares), rear crater (diamonds) and hole (filled circles) for different shots in our impact experiments and distinct thickness (T_R). A rear crater diameter of T_C=4 cm is defined as the maximum size of the crater because the shape of the rear crater is occasionally ellipsoidal, as a result of the restriction of the narrow cavity when T_C is 4 cm. Refer to Table 1 for more details. In our experiments, T_R=6 cm represents targets without cavity.

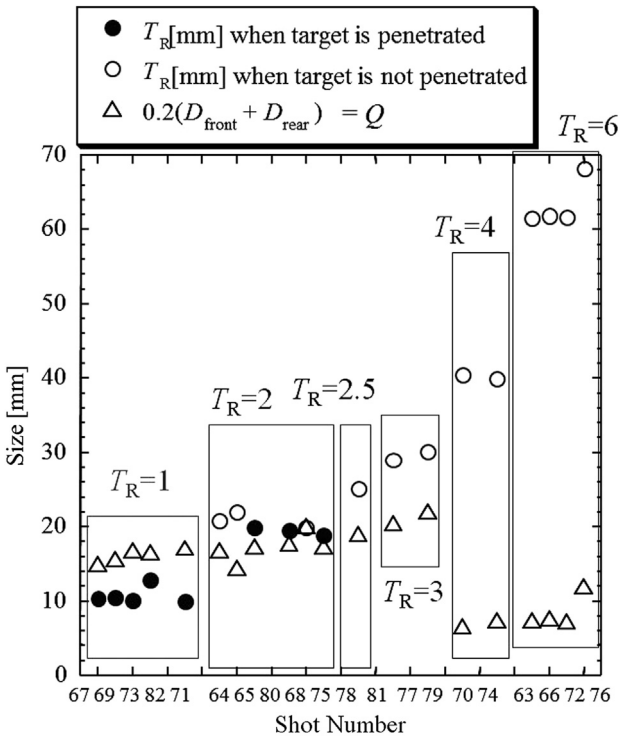

Fig. 5. Relationship between target thickness, hole size, and the sum of the estimated depths in the front crater and the rear crater. The sum of the front crater and rear crater diameters multiplied by 0.2, defined as Q, is indicated by triangles. Filled circles indicate the target thickness when the target is penetrated, unfilled circles show target thickness where no penetration occurs. For a hole to be observed, the condition $Q > T_R$ must be satisfied.

contain some fragments shed from the side of the target, because the surface on the side of the target crumbles due to the vibration following the impact. Besides, some of the fragments drop when the target is removed from the target holder. Therefore, it is difficult to distinguish the impact ejecta from other fragments. In the following, the collected total ejecta mass from the front and the rear craters is abbreviated as M_c, and the difference in target mass measured before and after the impact is abbreviated as M_f. The ratio of M_c to M_f is defined as the ejecta mass collection ratio. This ratio varies from 20% to 80% (with an average of approximately 50%). The main cause of what looks like a low collection ratio is probably the overestimation of M_f as the target mass is reduced by fragments from the side of the target. Thus, the underestimation of the target mass after the impact resulted in an overestimation of M_f. Another contribution towards the underestimation of M_c was that some ejecta were lost into a narrow opening space. However, this contribution was minor because the narrow opening space is very small (a few mm). Therefore, the actual collection ratio can be assumed to be near 80%, considering the fragments from the side of the target.

We measured the amount of ejecta from the front crater and those from the rear crater separately. In those impact cases where only front craters are formed (T_R=4 and 6 cm), the ratio of the amount of ejecta from the front crater to M_c is larger than 95%. On the other hand, in those impact cases where both front and rear crater are formed ($T_R \leq 3$ cm), most of the ejecta originally came from the rear crater, yielding ratios ranging from 70% to 90%. These ratios appear to be independent of target thickness; e.g., the ratios are 69–88% for T_R=3 cm and 65–84% for T_R=1 cm, respectively. Thus, when both front and rear crater are formed, the targets seem to be characterized by a higher proportion of fragments being ejected from the rear crater than from the front crater. In our experiments, we could not distinguish the origin of some 20% of the ejecta (i.e., front or rear crater), and this portion of the total collected ejecta mass was excluded from the analysis.

Using the images of the high-speed camera, we found that the excavation flow of the front craters behaved in a similar way for all targets. The fragments were ejected at an angle of almost 45° relative to the impact surface. In contrast, the rear crater fragments were ejected vertically. This may be caused by the target holder which partially masks the rear surface.

3.3. Antipodal velocity and pressure

As mentioned above, the high pressure in a shock wave is relieved by the propagation of rarefaction, which controls the shape of craters. The formation of the rear crater depends largely on the pressure of the rarefaction at the rear surface (antipodal pressure). One of aims is to estimate the antipodal pressure because it influences rear crater and hole formation. We estimate the antipodal pressures of our experiments using the antipodal velocities, i.e. the velocities of the fastest fragments ejected from the rear crater, a method applied for instance, by Arakawa (1999).

In our experiments, antipodal velocities were obtained from the images of a one-directional camera taken through the side windows of the chamber. It is therefore possible that we underestimate the antipodal velocities if the ejection angle of the fragments at the antipodal point is not perpendicular to the rear target surface. However, the ejection angle of the fragments at the antipodal point is most likely to be perpendicular to the rear target surface. In shot number 82, the target was rotated 45° and the projectile hit the surface at this angle. The fragments near the antipodal point were ejected perpendicularly into the rear target surface.

Fig. 6 shows the relationship between antipodal velocity and the target thickness. The antipodal velocity (V_a) decreases from 270 m/s to 8 m/s with increasing thickness. From our data in Fig. 6, this relation can be described by

$$V_a = 2.6 \times 10^2 \times T_R^{-3}, \quad (1)$$

and it is used to estimate the attenuation of shock pressure. The antipodal shock pressure (P) is calculated from

$$P = \rho C V_a / 2, \quad (2)$$

where ρ is the density of the target, and C is the bulk sound velocity of the target (e.g., Arakawa, 1999). This equation is applicable when the antipodal velocity is less than the bulk sound velocity in the target. We measured a bulk sound velocity of $C = 2280 \pm 60$ m/s in our targets. This value was obtained from measurements of the arrival time of pulse waves in the target. From Eqs. (1) and (2), the antipodal pressure as a function of target thickness can now be estimated as

$$P = 1.3 \times 10^2 \times \rho C \times T_R^{-3}. \quad (3)$$

Note that the shock pressure attenuation depends on impact velocity (e.g., Holsapple, 1993). The higher the impact velocity, the faster the shock waves decay. In general, the evolution of shock waves is divided into three distinct regimes, depending on the magnitude of the pressure. Holsapple (1993) defines these three regimes as 'strong-shock regime', where the pressure $P \gg \rho C^2$, 'intermediate regime', where the pressure $P \sim \rho C^2$, and 'weak shock regime', where $P \sim Y$, Y being the 'material strength'. In our experiments, the impact velocity is smaller than the bulk sound velocity of the target, which means that the evolution of the shock wave is in the intermediate regime or less. Therefore, if the impact velocity is somewhat larger than that of our experiments, it is possible that the shock wave attenuation becomes steeper.

Using Eq. (3) with $\rho = 1550$ kg/m^3 and $C = 2280$ m/s, the relationship between antipodal pressure and target thickness is shown in Fig. 7. The horizontal solid line indicates the compressive strength of the target. Fig. 7 shows that rear craters are produced when the antipodal pressure is greater than the target strength, although there may be considerable uncertainty in the value for the antipodal pressure.

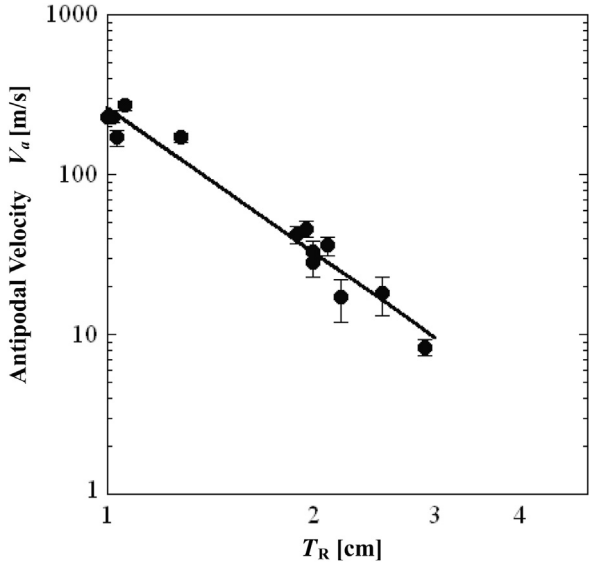

Fig. 6. Relationship between antipodal velocity and target thickness (T_R). Filled circles represent the antipodal velocity. The solid line indicates a linear regression of these data, and can be expressed as $V_a = 2.6 \times 10^2 \times T_R^{-3}$, where V_a is the antipodal velocity.

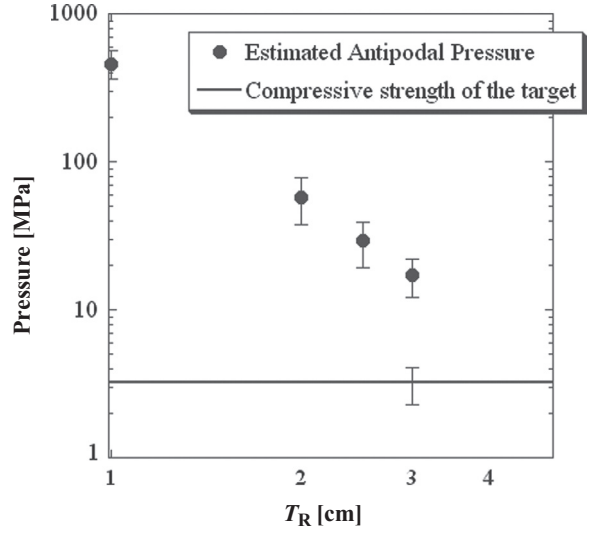

Fig. 7. Relationship between antipodal pressure and target thickness (T_R). Filled circles show the estimated antipodal pressure using Eq. (3) with $\rho = 1550$ kg/m^3 and $C = 2280$ m/s. The horizontal solid line indicates the compressive strength of the target. Rear craters are produced when $T_R \leq 3$ cm.

4. Discussion

4.1. Comparison with other material targets

In our experiments with brittle targets, a rear crater was produced as a result of the rarefaction originating at the opposite side of the impact; this happened even when no target penetration occurred. In contrast, the penetration process of metal targets is different from what we observed in our experiments on brittle targets. Hörz et al. (1994, 1995, 2012) carried out impact experiments for Aluminum and Teflon targets of widely variable thickness ranging from microns to centimeters and investigated the transition from cratering to penetration. They employed spherical soda-lime glass projectiles of 50–3175 μm at impact velocities from 1 to 7 km/s. For Aluminum, the cross section showed a ductile deformation behavior, and a rear crater was not produced (cf. Figure 11 in Hörz, 2012). For Teflon, the cross section showed intermediate behavior between ductile and brittle, and a rear crater was produced when target penetration occurred (cf. Figure 20 in Hörz, 2012). However, a rear crater was not produced when target penetration did not occur, although some cracks appeared at the opposite side of the impact. Our experiments therefore indicate that rear craters are more easily produced in brittle targets than in metal targets.

The shock pressure attenuation would affect the thickness of the layer between the front and the rear craters. In the previous section, the pressure attenuation of our experiment was estimated as $P \propto r^{-3}$, where P and r are shock pressure and propagation distance, respectively. The value of our pressure attenuation coincides with the one adopted by Mizutani et al. (1990), which was obtained from the experimental data of a series of nuclear explosions. Although the shock pressure attenuation in the far field has been discussed by many authors, there are large variations in published results. Dence et al. (1977) observationally examined the distribution of shock metamorphism in rocks below natural impact craters. They estimated the pressure attenuation as $P \propto r^{-2}$–$r^{-4.5}$. Nakazawa et al. (2002) measured the shock pressure attenuation in basalt. They examined the shock wave attenuation by employing in-material manganin and carbon pressure gauges. In their experiments, shock waves of 7 and 31 GPa were generated using a thin flyer plate, and a shock wave of 16 GPa was generated using a thick cylindrical projectile. Nakazawa et al. (2002) found a pressure attenuation of $P \propto r^{-1.7}$–$r^{-1.8}$. Shirai et al. (2008) measured the shock pressure profile in water ice at various distances from the impact point. They found the pressure to be attenuated as $P \propto r^{-2.2}$. Our targets

are more porous than the materials used in the above experiments. Therefore, one would expect the shock wave to attenuate more rapidly ($P \propto r^{-3}$) in our experiments than in those of the above authors.

The shape of an impact crater is also affected by target porosity, strength and projectile-to-target density ratio. For example, Michikami et al. (2007) carried out impact cratering experiments on sintered glass-bead targets with various porosities (from ~7% to 80%) and compressive strengths (from ~0.5 to 250 MPa) using spherical alumina projectiles. The least porous and strongest target (porosity~7% and compressive strength ~250 MPa) yielded the shallowest crater, and the most porous and weakest one (porosity ~80% and compressive strength ~0.5 MPa) was penetrated most deeply. In their experiments, although crater *size* depends on the material strength of the target (there is also a slight porosity dependence), crater *shape* (especially the depth/diameter ratio of a crater) strongly depends on the density ratio of the projectile to the target. In general, craters in consolidated (as opposed to lose) material were found to be very deep when the density of the projectile was significantly large compared to the density of the target (e.g., Love et al., 1993, Michikami et al., 2007, Poelchau et al., 2013). For instance, the depth/diameter ratio of a crater is approximately 4 for a projectile/target density ratio of approximately 9 (cf. shot number 513 in Michikami et al., 2007). More recently, the effects of target porosity on both crater *size* and crater *shape* were investigated by Poelchau et al. (2013). They carried out impact cratering experiments on porous wet and dry sandstone targets using steel, iron meteorite, and aluminum projectiles. Their results show that the target porosity reduces crater volume and cratering efficiency (the ratio of excavated mass to projectile mass) relative to nonporous rocks. However, the effect of porosity on crater *shape* (the depth/diameter ratio of a crater) is not clearly visible when their shots into dry sandstones are compared with impacts in nonporous brittle materials (cf. Figure 4 in Poelchau et al., 2013).

Although target porosity, strength and target-to-projectile density ratio influence the crater formation, we assumed these influences to be less relevant because the projectile (or impactor) and the target (or surface layer) are unlikely to differ dramatically in terms of porosity, strength and density when considering impacts on planets.

4.2. Implications for deep pit craters on Mars

Although relating our laboratory experiments to real collisions in space may not be straightforward, the data presented here can provide important evidence to interpret the existence of deep pit craters on Mars. Crater formation is generally divided into two regimes, the strength and the gravity regime, depending on which of the two effects dominates during cratering.

To relate our experiments to the formation of the deep pit craters on Mars, the scaling law of Holsapple (1993) is used because this law applies to impact cratering in a wide range of gravity and is adopted by many authors (e.g., Poelchau et al., 2013). Holsapple (1993) gave a generalized equation for the cratering efficiency (π_V):

$$\pi_V = K\left(\pi_2 + \pi_3^{\frac{2+\mu}{2}}\right)^{-\frac{3\mu}{2+\mu}}, \quad (4)$$

where π_2 and π_3 are the gravity-scaled and strength-scaled size parameters, respectively; the coefficients of K and μ can be determined from the experimental data (for more detail, see figure caption in Fig. 8). Fig. 8 shows the cratering efficiency of our experiments using the scaling law of Holsapple (1993). In the strength regime the cratering efficiency is constant but depends on the impact velocity. In the gravity regime, the cratering efficiency decreases with increasing impactor size. The exponent of this decrease was estimated to be 0.75 because the cratering efficiency of our experiments was proportional to the impact energy. The deep pit craters detected so far on Mars are 100–250 m in diameter (Cushing et al., 2007). Craters in this size range are considered to form in the strength regime because the value of π_2 (see Fig. 8) would be small enough. Thus, our experimental results can be applied to these craters.

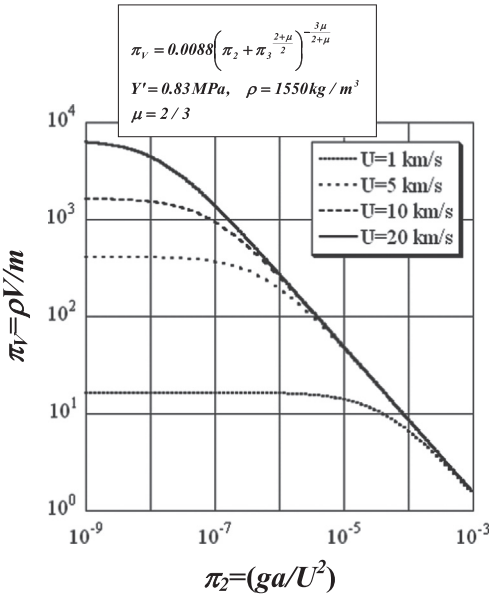

Fig. 8. Cratering efficiency π_V of our experiments using the scaling law of Holsapple (1993) obtained from shots into targets without a cavity (s63, s66, s72 and s76 for T_R=6 cm). Horizontal and vertical axes indicate the gravity-scaled size parameter π_2 and the cratering efficiency π_V, respectively: g is gravity acceleration, a is the impactor size, U is the impact velocity, ρ is the target's density, m is the impactor's mass. The crater volume V is estimated to be $0.66R^3$, where R is the radius of the crater (the depth of the crater is $0.4R$ from the results of the experiments). The coefficients of K and μ can be determined from the experimental data in the used target material. When the impact cratering is in the strength regime, the gravity-scaled size parameter π_2 is negligible. In this case, Eq. (4) can be rewritten as

$$\pi_V = K{\pi_3}^{-3\mu/2}, \quad (4')$$

where π_3 ($=Y/\rho U^2$) is a strength-scaled size parameter: in our experiments, the effective strength Y is assumed to be the tensile strength of the target (0.83 MPa) for simplicity, ρ is 1550 kg/m^3, and the values of U range from 1.22 to 2.70 km/s (T_R=6 cm). A linear regression of these data (T_R=6 cm) using Eq. (4′)) yields the values shown, with K=0.0088 and μ=2/3. Thus, the exponent $(3\mu/(2+\mu))$ in the gravity regime can be estimated as 0.75.

In most of our impact experiments (except for shot 82), the projectiles were shot perpendicularly into the target surface, but such impacts onto the planetary surfaces are rare. In general, the impact angle does not affect the crater shape significantly, except for the highest angles of glancing incidence. Burchell and Whitehorn (2003) carried out impact experiments into granite rocks at a mean impact velocity of 5.4 ± 0.2 km/s, with an impact angle ranging from 0° (vertical incidence) to 85° (glancing incidence). Their data show nearly constant crater shapes until the angle of impact exceeds 50° measured from the vertical. Elbeshausen et al. (2009) developed iSALE-3D, a three-dimensional multi-rheology hydrocode, and showed that existing scaling laws in principle describe oblique planetary-scale impact events at angles smaller than 60° measured from the vertical. Before these studies, some studies of oblique cratering were well summarized by Pierazzo and Melosh (2000) who showed that melting and vaporization depend on impact angle. In our experiments, only shot 82 was carried out with an impact angle of 45°

relative to the target surface, to confirm the effect of the impact angle on the crater shape. The crater shapes obtained are similar as for targets of the same roof thickness. It is therefore reasonable to conclude that the crater shape is independent of impact angle in this range (0°–45°), although investigations for the highest angles from the vertical would be needed in the future.

On the Moon, three giant deep pit craters (Marius Hills pit, Mare Tranquillitatis pit and Mare Ingenii pit) were identified in SELenological and ENgineering Explorer (SELENE) Terrain Camera images (Haruyama et al., 2009, 2010). These Lunar deep pit craters with 53–93 m in mean diameter have depths ranging from 37 to 107 m (Robinson et al., 2012). More than 150 additional, smaller pits, of various shapes and sizes, were identified in Lunar Reconnaissance Orbiter Camera (LROC) (Robinson et al., 2010). However, in spite of Lunar global mapping data of SELENE, there are only three known deep pit craters larger than 50 m on the Moon, significantly fewer than on Mars in this size range. Further studies are necessary in order to understand why deep pit craters larger than 50 m on the Moon are so rare.

Martian deep pit craters with diameters between 100 and 250 m have depths ranging from 68 to 172 m, although some of their depths have not yet been determined (Cushing et al., 2007). Indeed, the exact cross sections of these deep pit craters are poorly known because spacecraft image data at limited solar incident angles are not sufficient to determine their shapes. However, the cross sections of some deep pit craters on Mars seem to be similar to those of craters with a hole obtained in our experiments.

Penetration of the target was achieved when the craters of both the impact and the opposite side were connected, with the crater shape resembling a flat hourglass. The threshold for penetration, called ballistic limit, is an important parameter for understanding the cross section of Martian deep pit craters. In our experiments for $T_R=2$ cm, we found targets with and without holes. Therefore, we could reasonably set the ballistic limit at $T_R=2$ cm. In these cases, the mean diameter (D_C) of six front craters for $T_R=2$ cm is 3.3 cm. Thus, the value of T_R/D_C at the ballistic limit of our experiments is 0.6 ($=2/3.3$). As mentioned before, the cross sections of Martian deep pit craters are poorly known, but the cross sections of Lunar giant deep pit craters have been modeled by Robinson et al. (2012). A hypothesis is that these deep pit craters were produced by the collapse of the roofs of lava tubes. For instance, Robinson et al. (2012) inferred that Marius Hills pit has a roof thickness (T) of 26 m and a diameter (D_C) of 53 m. If this deep pit crater was produced by one impact event and there is no ensuing collapse of the ceiling, the T/D_C ratio is 0.49 for simplicity, which is below the ballistic limit of our experiments. A similar ratio is seen on Mare Tranquillitatis pit. Therefore, the T_R/D_c ratio at the ballistic limit of our experiments corresponds with the ratio inferred from the observed shapes of Lunar giant deep pit craters.

In case the formation of Lunar giant deep pit crater was triggered by an impact event and followed by a collapse of the ceiling, the ballistic limit would be different from the value of $T/D_C=0.49$ estimated above. Considering this effect, Martellato et al., 2013 investigated the possible impact formation of deep pit craters on the Moon by computer simulations using basalt as a material for both the projectile and the target. They showed that the T/D_C ratio at the ballistic limit for planetary scales is around one. This ratio is larger than that of the ballistic limit at lunar-like impact velocities, which is based on laboratory impact experiments with Teflon and Aluminum targets (cf. Figure 13, in Hörz 2012). Martellato et al., 2013 indicated that Marius Hills pit was produced by a crater with a diameter 40 m in a 26 m thick target, and Mare Tranquillitatis was produced by a crater with a diameter 75.6 m in a 47 m thick target. They presented that the target thickness-to-crater diameter ratio is 0.65 ($=26/40$) and 0.62 ($=47/75.6$), for Marius Hills pit and Mare Tranquillitatis pit respectively. The ratios for both of these pits which are below the ballistic limit of their simulations, are similar to those of our experiments at the ballistic limit.

We now explore two scenarios for the formation of deep pit craters related to impact events. Cushing et al. (2007) suggested that Martian deep pit craters are not of impact origin because they lack the raised rims and impact ejecta. A similar proposition about Lunar deep pit craters was made by Robinson et al. (2012), but they did not rule out that deep pit craters were triggered by an impact event and subsequent collapse of the ceiling. In *Scenario A*, the formation of a deep pit crater is triggered by an impact event, and followed by collapse of the ceiling. In images, many blocks are distributed across the floor of Lunar and Martian deep pit craters, and likely represent fragments from the pit walls or collapsed roof materials (Robinson et al., 2012). In our experiments, rear craters are formed even when no target penetration occurs, and their diameters are larger than those of the front craters. This result support *Scenario A* as follows. If the collapse of the ceiling continues after the formation of the crater, the collapse may progress until the diameter of the deep pit crater equals that of the rear crater, which implies that the surface morphological signature of the front crater is effectively removed. This may indicate that even a rim of a front crater could collapse into the cavity long after the formation of an original crater, which explains why some deep pit craters lack crater rims. We now move on to *Scenario B,* in which a deep pit crater is produced solely by one impact event into a subsurface cavity, with no subsequent collapse of the ceiling. In our experiments, more fragments are ejected from the rear crater than from the front crater. The mass ratio of fragments from the rear crater to all fragments ranges from 70% to 90%. Only very few fragments are ejected from the front, and these are ejected at a wide angle compared with the fragments from the rear crater. This result would support not only *Scenario A* but also *Scenario B*. In general, crater rims on planets topographically consist of ejecta materials and structural uplift of the underlying preimpact surface (Melosh, 1989). If the amount of ejecta on the surface is small and the roof thickness of the planetary subsurface is thin, as seen on our experiments, the crater rim might become very small. Thus, our experimental results support both scenarios. Currently, there is no imagery available to confirm the presence – or lack – of shape characteristics such as the flat hour-glass profile seen in our experiments. Whether this shape exists in any of the deep pit crater ceilings, or whether it has disappeared as the target ceilings collapsed over time, can only be found out once we know more about the morphology of deep pit craters.

5. Conclusions

We investigated the effect of brittle target thickness T_R on crater formation to understand the conditions for the transition from target cratering to target penetration. We observed that rear craters are formed even when no target penetration occurs, a result that has not been observed in similar experiments on metal targets. When both front and rear craters were connected, the cross section of the combined crater attained a flat hourglass-like shape and the target was penetrated. The transition from target cratering to target penetration occurred at a target thickness of $T_R=2$ cm. While the diameter of front craters remained almost constant, regardless of target roof thickness and cavity width, rear crater diameters increased with target roof thickness, and were considerably larger than the diameters of the front craters in those targets with 1 cm $\leq T_R \leq$ 3 cm. The value of T_R/D_C at the ballistic limit of our experiments is 0.6, which is less than the value estimated by Martellato et al. (2013) on the Moon.

When both front and rear craters were formed ($T_R \leq 3$ cm), more fragments were ejected from the rear crater (yielding ratios ranging from 70% to 90%) than from the front crater. These ratios appear to be independent of target thickness. Using a high-speed camera, we found that the excavation flow of both the front and the rear craters behaved in a similar way for all targets. The fragments were ejected at an angle of almost 45° relative to the impact surface. In contrast, the rear crater fragments were ejected vertically.

We can apply our results to some deep pit craters found on Mars. The cross sections of some of these craters on Mars, although not very accurately known, appear to be similar to those craters with a hole from our experiments. Most deep pit craters on Mars lack crater rims and many blocks are distributed across their floors. We have presented two simple scenarios that relate these observations to the impact origin of these craters. In *Scenario A*, the formation of a deep pit crater was triggered by an impact event followed by the collapse of the ceiling, supported by our observation that rear craters are formed even when no target penetration occurs. As their diameters are larger than those of the front craters, the collapse of the remaining ceiling may progress until the diameter of the deep pit crater equals that of the rear crater, which implies that the crater rim is effectively removed. Our *Scenario B* assumes that a deep pit crater was produced solely by one impact event. Our experiments showed that more fragments are ejected from the rear crater than from the front crater, which would support not only *Scenario A* but also *Scenario B* because any crater rim would be very small as a result of both the small amount of ejecta from the front crater and the roof being too thin. In supporting both of these scenarios, our results provide a qualitative explanation for the observation that the deep pit craters of Mars lack raised rims and have ejecta deposits on their floor instead.

Acknowledgments

The authors acknowledge S. Hasegawa's and N. Hirata's help, provided in useful discussions and suggestions. We also thank H. Shiraishi, M. Yamanouchi and T. Midorikawa for the support of our strength measurements. This paper was significantly improved by the comments from an anonymous reviewer. A. Hagermann was supported by STFC and the UK Space Agency. The experiments were conducted and supported by the Space Plasma Laboratory, ISAS, JAXA, and Fukushima Prefectural Foundation for Promotion of Research and Education.

References

Arakawa, M., 1999. Collisional disruption of ice by high-velocity impact. Icarus 142, 34–45.
Banerdt, W.B., Golombek, M.P., Tanaka, K.L., 1992. Stress and tectonics on Mars. In: Kieffer, H.H., Jakosky, B.M., Snyder, C.M., Matthews, M.S. (Eds.), Mars. University of Arizona Press, Tucson, pp. 249–297.
Bleamaster, L.F., Hansen, V.L., 2004. Effects of crustal heterogeneity on the morphology of chasmata, Venus. J. Geophys. Res. 109, E02004, http://dx.doi.org/10.1029/2003JE002193.
Burchell, M.J., Whitehorn, L., 2003. Oblique incidence hypervelocity impacts on rock. Mon. Not. R. Astron. Soc. 341, 192–198.
Cushing, G.E., Titus, T.N., Wynne, J.J., Christensen, P.R., 2007. THEMIS observes possible cave skylights on Mars. LPSC XXXVIII, No. 1371.
Cushing, G.E., 2012. Candidate cave entrances on Mars. J. Cave Karst Stud. 74, 33–47.
Dence, M.R., Grieve, R.A.F., Robertson, P.B., 1977. Terrestrial impact structures: principal characteristics and energy considerations. In: Roddy, D.J., Pepin, R.O., Merrill, R.B. (Eds.), Impact and Explosion Cratering. Pergamon Press, NewYork, pp. 247-275.
Elbeshausen, D., Wünnemann, K., Collins, G.S., 2009. Scaling of oblique impacts in frictional targets: implications for crater size and formation mechanisms. Icarus 204, 716–731.
Ferrill, D.A., Wyrick, D.Y., Morris, A.P., Sims, D.W., Franklin, N.M., 2004. Dilational fault slip and pit chain formation on Mars. Geol. Soc. Am. 14 (10), 4–12.
Haruyama, J., Hioki, K., Shirao, M., Morota, T., Hiesinger, H., van der Bogert, C.H., Miyamoto, H., Iwasaki, A., Yokota, Y., Ohtake, M., Matsunaga, M., Hara, S., Nakanotani, S., Pieters, C.M., 2009. Possible lunar lava tube skylight observed by SELENE cameras. Geophys. Res. Lett. 36, L21206, http://dx.doi.org/10.1029/2009GL040635.
Haruyama, J., Morota, T., Kobayashi, S., Sawai, S., Lucey, P.G., Shirao, M., Nishino, M. N., 2012. Lunar holes and lava tubes as resources for lunar science and exploration. In: Badescu, V. (Ed.), Moon – Prospective Energy and Material Resources. Springer Berlin Heidelberg, pp. 139–163
Head, J.W., Wilson, L., 1993. Lunar graben formation due to near-surface deformation accompanying dike emplacement. Planet Space Sci. 41, 719–727.
Holsapple, K.R., 1993. The scaling of impact processes in planetary science. Ann. Rev. Earth Planet. Sci. 21, 333–373.
Hörz, F., Cintala, M.J., Bernhard, R.P., See, T.H., 1994. Penetration experiments in aluminum and teflon targets of widely variable thickness. In: Lunar and Planetary Institute, Workshop on Particle Capture, Recovery and Velocity/Trajectory Measurement Technologies, pp. 42–48.
Hörz, F., Cintala, M.J., Bernhard, R.P., See, T.H., 1995. Cratering and penetration experiments in teflon targets at velocities from 1 to 7 km/s. Int. J. Impact Eng. 17, 419–430.
Hörz, F., 2012. Cratering and penetration experiments in aluminum and teflon: implications for space-exposed surfaces. Meteor Planet. Sci. 47, 763–797.
Horstmann, K.C., Melosh, J.H., 1989. Drainage pits in cohensionless materials: implications for the surface of Phobos. J. Geophys. Res. 94, 12433–12441.
Housen, K.R., Holsapple, K.A., 1999. Scale effects in strength-dominated collisions of rocky asteroids. Icarus 142, 21–33.
Love, S.G., Hörz, F., Brownlee, D.E., 1993. Target porosity effects in impact cratering and collisional disruption. Icarus 105, 216–224.
Martellato, E., Foing, B.H., Benkhoff, J., 2013. Numerical modeling of impact crater formation associated with isolated lunar skylight candidates on lava tubes. Planet Space Sci. 86, 33–44.
Melosh, H.J., 1989. Impact Cratering: A Geologic Process. Oxford University Press, New York.
Michikami, T., Moriguchi, K., Hasegawa, S., Fujiwara, A., 2007. Ejecta velocity distribution for impact cratering on porous and low strength targets. Planet Space Sci. 55, 70–88.
Mizutani, H., Takagi, Y., Kawakami, S., 1990. New scaling law on impact fragmentation. Icarus 87, 307–329.
Nakazawa, S., Watanabe, S., Iijima, Y., Kato, M., 2002. Experimental investigation of shock wave attenuation in basalt. Icarus 156, 539–550.
Okubo, C.H., Martel, S.J., 1998. Pit crater formation on Kilauea volcano, Hawaii. J. Volcanol. Geotherm. Res. 86, 1–18.
Pierazzo, E., Melosh, H.J., 2000. Understanding oblique impacts from experiments, observations, and modeling. Ann. Rev. Earth Planet. Sci. 28, 141–167.
Pike, R. J., 1977. Size-dependence in the shape of fresh impact craters on the Moon. In: Roddy, D.J., Pepin, R.O., Merrill, R.B. (Eds.), Impact and Explosion Cratering. Pergamon Press, ,NewYork,pp.489–509.
Pike, R. J., 1988. Geomorphology of impact craters on Mercury. In: Vilas, F., Chapman, C.R., Matthews, M.S., (Eds.), Mercury. University of Arizona Press, Tucson,pp.165–273.
Poelchau, M.H., Kenkmann, T., Thoma, K., Hoerth, T., Dufresne, A., Schäfer, F., 2013. The MEMIN research unit: scaling impact cratering experiments in porous sandstones. Meteor. Planet. Sci. 48, 8–22.
Prockter, L., Thomas, P., Robinson, M., Joseph, J., Milne, A., Bussey, B., Veverka, J., Cheng, A., 2002. Surface expressions of structural features on Eros. Icarus 155, 75–93.
Robinson, M.S., Brylow, S.M., Tschimmel, M., Humm, D., Lawrence, S.J., Thomas, P.C., Denevi, B.W., Bowman-Cisneros, E., Zerr, J., Ravine, M.A., Caplinger, M.A., Ghaemi, F.T., Schaffner, J.A., Malin, M.C., Mahanti, P., Bartels, A., Anderson, J., Tran, T.N., Eliason, E.M., McEwen, A.S., Turtle, E., Jolliff, B.L., Hiesinger, H., 2010. Lunar Reconnaissance Orbiter Camera (LROC) instrument overview. Space Sci. Rev. 150 (1–4), 81–124.
Robinson, M.S., Ashley, J.W., Boyd, A.K., Wagner, R.V., Speyerer, E.J., Ray Hawke, B., Hiesinger, H., van der Bogert, C.H., 2012. Confirmation of sublunarean voids and thin layer in mare deposits. Planet Space Sci. 69, 18–27.
Shirai, K., Kato, M., Mitani, N.K., Arakawa, M., 2008. Laboratory impact experiments and numerical simulations on shock pressure attenuation in water ice. J. Geophys. Res. 113, E11002, http://dx.doi.org/10.1029/2008JE003121.
Thomas, P., 1979. Surface features of Phobos and Deimos. Icarus 40, 223–243.
Wang, Q.Z., Li, W., Song, X.L., 2006. A method for testing dynamic tensile strength and elastic modulus of rock materials using SHPB. Pure appl. Geophys. 163, 1091–1100.
Wilson, L., Head III, J.W., 2002. Tharsis-radial graben systems as the surface manifestation of plume-related dike intrusion complexes: models and implications. J. Geophys. Res. 107 (E8), 5057, http://dx.doi.org/10.1029/2001JE001593.
Wyrick, D., Ferrill, D.A., Morris, A.P., Colton, S.L., Sims, D.W., 2004. Distribution, morphology, and origins of Martian pit crater chains. J. Geophys. Res. 109, E06005, http://dx.doi.org/10.1029/2004JE002240.